

Plant-mediated green synthesis of nanocomposite-based multifunctional adsorbent with antibacterial activity and high removal efficiency of micropollutants from contaminated waters

Payam Arabkhani ^a, Arash Asfaram ^{a,*}, Mojtaba Aghaei-Jazeh ^b, Mohamed Ateia ^c

^a Medicinal Plants Research Center, Yasuj University of Medical Sciences, Yasuj, Iran

^b Department of Microbiology, Varamin Branch, Islamic Azad University, Tehran, Iran

^c Department of Chemistry, Northwestern University, Evanston, IL 60208, USA

ARTICLE INFO

Keywords:

Acetaminophen
Antibacterial activities
Green synthesis
Multifunctional nanocomposite
Paraquat herbicide

ABSTRACT

Wastewaters are contaminated with both biological and chemical pollutants that must be eliminated before reuse and/or disposal to surface waters. This paper proposes a new magnetic CuO-doped silver/polyacrylonitrile/zeolitic imidazolate framework-67 nanocomposite (M-CuO@Ag/PAN/ZIF-67) that has multifunctional behavior for removing acetaminophen (ACT) and paraquat (PQ) residuals from contaminated water while also acting as an antibacterial agent. The antibacterial agent of as-prepared nanocomposite on Gram-positive bacteria, *Staphylococcus-aureus* (*S. aureus*), and *Bacillus subtilis* (*B. subtilis*), and also Gram-negative bacteria *Escherichia coli* (*E. coli*) were studied. To minimize the use of harmful chemicals and solvents, Fe₃O₄, Ag, and CuO nanoparticles were prepared through plant-mediated green synthesis by renewable, and non-toxic aqueous extracts of *aloe vera* plant, mulberry leaves, and *Gundelia tournefortii* L, respectively. The adsorption results showed that the nanocomposite could remove 99.41 ± 2.21 % of the ACT and 99.23 ± 1.83 % of the PQ from the contaminated water. The Langmuir maximum adsorption capacity of ACT and PQ by nanocomposite was calculated as 971.6 and 1143.7 mg g⁻¹, respectively, which surpasses that of most nanocomposite-based adsorbents. Also, the adsorption kinetic data were well described with the pseudo-second-order model and the adsorption thermodynamic results showed the adsorption process was endothermic and spontaneous in nature. The antibacterial properties of nanocomposite were studied by pour plate and disk diffusion methods. It was concluded that bacterial suppression by the nanocomposite was higher in the Gram-positive bacteria than in the Gram-negative bacterium. The antibacterial results also showed that the collective antibacterial effects of the nanocomposite are stronger than its components and copper oxide-doped has also strengthened the antibacterial properties. In addition, the nanocomposite could be easily regenerated by washing with methanol, and chlorination method. Finally, the adsorption efficiency and antibacterial behavior of nanocomposite remained above 80 % and 90 % after six reuse cycles, respectively.

1. Introduction

Currently, the growth of the presence of various types of emerging pollutants in water such as pharmacological, pesticide, and bacterial pollutions have become a serious problem that greatly threatens the environment and millions of humans' health worldwide. Many of these pollutants in the environment, even in low concentrations, cause mutagenicity, biological responses, and adverse effects on human health and other living organisms [1,2]. Therefore, the elimination of these pollutants and preventing their release into the environment is of

particular importance. Acetaminophen (ACT), most known as paracetamol, is widely used as a painkiller and antipyretic worldwide [3]. Continuous exposure to ACT can lead to serious illness and injuries due to its toxic effects and must be removed from the effluents before being released into the environment [4]. Pesticides are often agrochemical compounds that are used to kill, repel, or control pests, and also increase productivity. Herbicides are a broad class of pesticides that are used to remove or inhibiting the growth of nuisance plants. Herbicides are of particular importance due to high solubility in water, toxicity, carcinogenicity, and mutagenic effects [5]. Paraquat (PQ), is one of the most

* Corresponding author.

E-mail address: arash.asfaram@yums.ac.ir (A. Asfaram).

toxic pesticides that is widely used as an herbicide in agriculture and its residues have been reported in water sources [6]. It is known that this PQ can cause fatal or severe physiological damage if deliberately or accidentally ingested. Therefore, its removal from water resources is very important [7]. On the other hand, bacteria are one of the most common types of microorganisms and bacterial contamination of drinking water is led to the spread of dangerous diseases and has become a major concern around the world, with thousands of people around the world dying each year related to the use of unsafe water. Gram-positive bacteria, *Bacillus subtilis* (*B. subtilis*), and *Staphylococcus aureus* (*S. aureus*), and Gram-negative bacteria *Escherichia coli* (*E. coli*) are among the bacteria commonly associated with the human environment. Water contaminated with these bacteria can cause a wide range of clinical diseases and in some cases even mortality [8]. The various methods including physical, chemical, membrane, biological treatment, and adsorption have been used for the treatment of unwanted pollutants from contaminated water [9]. Adsorption is considered a feasible, flexible, effective, simple operation, and economical technique to remove the wide range of pollution from water [10]. Over the past few years, researchers explored various adsorbents for ACT and PQ-contaminated waters treatment. However, there are still multiple challenges in the adsorption process, such as low adsorption capacity and regeneration of adsorbents. Therefore, choice of an efficient adsorbent is very important. In the last decades, the use of composites to remove pollutants from contaminated water has received much attention from researchers, and has been recognized that the nanocomposites fabricated by dispersing nanoparticles in polymer melts have a much better performance than traditional composites and may exhibit multifunctional behaviors [11]. The development of multifunctional nanocomposites by combining different nanomaterials and benefiting from their physical, chemical, and biological properties, can create more potential applications in the form of a cohesive structure [12]. Zeolitic imidazole framework-67 (ZIF-67) is one of the water stable metal-organic frameworks (MOFs) which have attractive properties

containing high surface area, high porosity, chemical stability, and simple synthesis and has been used in the treatment of many kinds of polluted water. Besides, some work demonstrated that the ZIF-67 show considerable bactericidal activity toward *S. aureus* and *E. coli* [13]. On the other hand, it is accepted that some metal and metal oxide nanoparticles show antibacterial behaviors. Among these materials, silver (Ag) and copper oxide (CuO) nanoparticles have attracted much attention and have been used in a variety of antibacterial activities [14]. The potent antibacterial properties of silver have led to its widespread use in medical applications. Nowadays, silver nanoparticles are used as effective nanomaterials against a wide range of bacteria [15]. The CuO structures have attracted a lot of attention in recent years due to their unique properties such as cheapness, very low toxicity, high antibacterial properties, high adsorption performance, and narrow bandwidth [16,17]. In recent years, researchers reported that the antibacterial activity of silver nanoparticles could be enhanced by combining with CuO nanoparticles [18].

In this paper, a magnetic CuO-doped silver/polyacrylonitrile/zeolitic imidazolate framework-67 nanocomposite (M-CuO@Ag/PAN/ZIF-67) was successfully synthesized by plant-mediated green synthesis methodology by renewable, and non-toxic aqueous extracts of *aloe vera* plant, mulberry leaves, and *Gundelia tournefortii* L. The overall schematic of the preparation steps has been illustrated in Fig. 1. Then, the application of as-prepared M-CuO@Ag/PAN/ZIF-67 in the adsorptive removal of PQ and ACT residues as well as the antibacterial effects on Gram-positive *S. aureus* and *B. subtilis* bacteria, and also Gram-negative *E. coli* bacteria were evaluated. In the adsorption process, the effects of independent variables including initial concentrations of ACT/PQ, solution pH, adsorbent mass, contact time, and solution temperature on ACT/PQ adsorption efficiency from aqueous solutions were determined and optimized. In addition, the antibacterial properties of M-CuO@Ag/PAN/ZIF-67 were studied by pour plate (Standard Method 9215B) and disk diffusion methods.

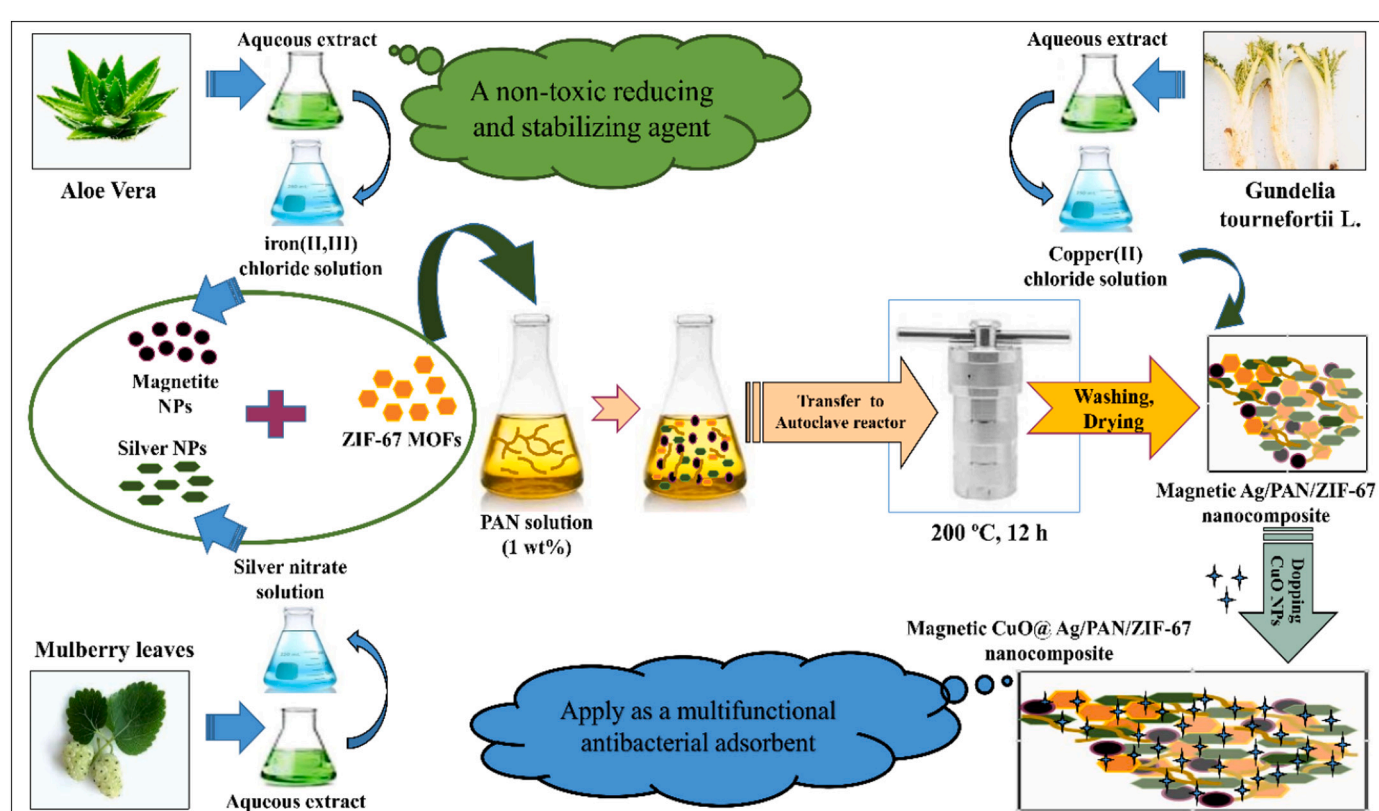


Fig. 1. Schematic illustration of the M-CuO@Ag/PAN/ZIF-67 preparation process.

2. Experimental

The chemicals, instruments, and preparation methods were all specified in the “Electronic Supplementary Information.”

2.1. Adsorption experiments

All the experiments were conducted in a lab-scale batch reactor, and the residual concentrations of ACT and PQ were analyzed using UV–Visible spectrophotometer at their maximum absorption wavelength of $\lambda_{\text{max}} = 243$ and $\lambda = 257$ nm, respectively. The adsorption capacity at equilibrium (q_e), each time (q_t), and the removal percentage ($R\%$) of the ACT and PQ were determined by the following equations [19,20]:

$$q_e = \frac{(C_0 - C_e)V}{m} \quad (1)$$

$$q_t = \frac{(C_0 - C_t)V}{m} \quad (2)$$

$$\text{MG removal (R\%)} = \frac{(C_0 - C_e)}{C_0} \times 100\% \quad (3)$$

where q_e (mg g^{-1}) shows the ACT/PQ adsorption amounts, q_t (mg g^{-1}) adsorption amounts at any time, C_0 (mg L^{-1}) and C_e (mg L^{-1}) the initial and equilibrium ACT/PQ concentrations, respectively, and C_t (mg L^{-1}) ACT/PQ concentrations at any time (t), V (L) volume of the ACT/PQ solutions, and m (g) denotes the mass of the adsorbent. In this study, the adsorption of ACT and PQ by nanocomposite was optimized using the CCD-RSM (Table S1) by Design Expert 7.0 software. In the optimization process, the responses were chosen based on a quadratic model. Also, the adsorption data were processed by analysis of variance (ANOVA) and the interaction between the independent variables and their responses were studied [21,22]. The independent variables affecting adsorption efficiency such as initial ACT/PQ concentrations, solution pH, adsorbent mass, sonication time (frequency: 20 kHz; power: 50 W), and solution temperature were investigated systematically with conducted 25 optimal number of experiments. The isotherm, kinetic, and thermodynamic studies were contended by the equilibrium experiments.

2.2. Antibacterial experiments

In this study, two different methods of pour plate (Standard Method 9215B) [23] and disk diffusion [18,24] methods were followed for the evaluation of the antibacterial activities of the as-prepared nanocomposite by applied the different concentrations (50–500 $\mu\text{g mL}^{-1}$). For antibacterial experiments, the three bacterial strains; gram-negative *Escherichia coli* (*E. coli*, ATCC-25922), gram-positive *Bacillus subtilis* (*B. subtilis*, ATCC-21332), and *Staphylococcus aureus* (*S. aureus*, ATCC-29213) were tested. In summary, in the pour plate method, a certain concentration of nanocomposite was mixed with sterilized warm (40–45 °C) Mueller Hinton agar (MHA). Also, 1 mL of diluted specimen bacterial suspension (1.0×10^9 CFU/mL) were poured into the sterile plate. Then, the warm agar was poured into the bacterial-containing plate and after the mixing, was allowed to solidify. Finally, plates were incubated for 24 h at 37 °C until bacterial colonies grow. Also, a control plate was also incubated for each bacterial strain without the addition of nanocomposite. In the disk diffusion method, the fresh bacteria cultures were prepared onto MHA plates. The antibiotic test discs (6 mm) impregnated with nanomaterials are then placed on the agar surface. Then, plates were incubated and the bacteria were allowed to grow completely for 24 h at 37 °C. Finally, the clear inhibition zones formed around the test discs were measured [25].

3. Result and discussion

3.1. Characterization

3.1.1. Crystallographic analysis

The phase purity and crystallinity of the prepared samples were studied by the XRD patterns and results are presented in Fig. 2. The characteristic diffraction peaks of ZIF-67 MOFs (Fig. 2a) showed that the resulted pattern was consistent with the reported pattern of ZIF-67 MOFs [26] and no extra peaks were observed. Also, the sharp peaks reveal the good crystallinity of ZIF-67 MOFs. The XRD pattern of as-synthesized Fe_3O_4 nanoparticles (Fig. 2b) shows good agreement with the data of cubic spinel Fe_3O_4 structure (JCPDS card no. 19-0629) [27]. The XRD pattern of the as-synthesized Ag nanoparticles (Fig. 2c) shows the characteristics peaks around 38.1° (111) and 44.2° (200), which is in good agreement with the face-centered-cubic form of metallic silver (JCPDS card no. 04-0783) [28]. The XRD pattern of pure PAN (Fig. 2d) shows a sharp crystalline peak at 17.1° (110), corresponding to orthorhombic PAN reflection. The XRD pattern of the M-Ag/PAN/ZIF-67 (Fig. 2e) well-matched with the naked ZIF-67 MOFs, Fe_3O_4 NPs, Ag NPs, and PAN polymer patterns. No extra peaks were observed due to the purity of the synthesized nanocomposite, and all the peaks were at the right place despite a slight shifting due to interactions between each other. In the XRD pattern of M-CuO@Ag/PAN/ZIF-67 (Fig. 2f), the new diffraction peaks have appeared at 36° (002) and 39.7° (200) along with other peaks related to M-Ag/PAN/ZIF-67. The appeared new peaks can be indexed to cubic crystalline phase of CuO (JCPDS card no. 78-0428) [29], which confirm the successful doping of CuO NPs on M-Ag/PAN/ZIF-67. In addition, the average crystallite size of nanocomposite was calculated using Scherrer's equation [30] and was determined to be

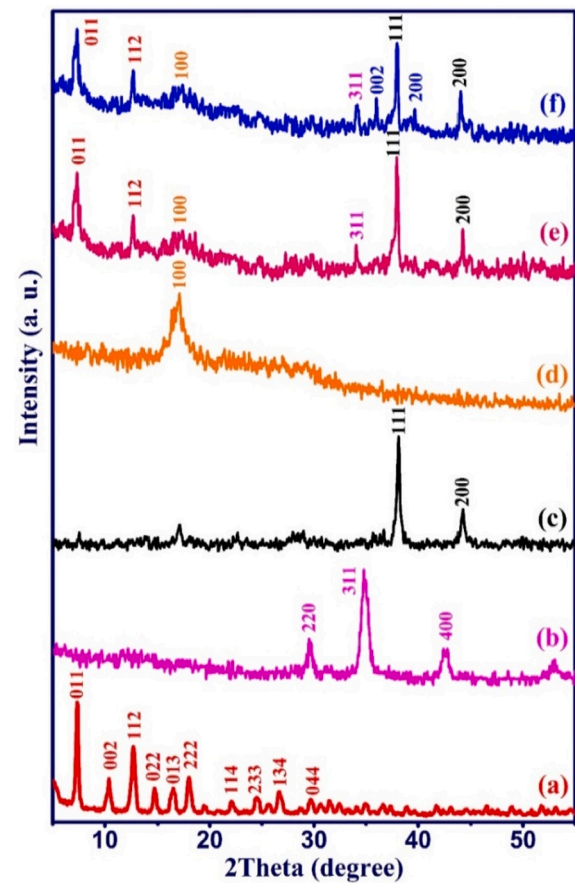


Fig. 2. XRD patterns of (a) ZIF-67 MOFs, (b) Fe_3O_4 NPs, (c) Ag NPs, (d) pure PAN polymer, (e) M-Ag/PAN/ZIF-67, and (f) M-CuO@Ag/PAN/ZIF-67.

35.5 nm.

3.1.2. Surface functional groups analysis

The surface functional groups of prepared samples were identified by FTIR analysis, and results are shown in Fig. S1. For ZIF-67 MOFs (Fig. S1a), the vibrational bands in the range of 600–1300 cm⁻¹, and 1355 cm⁻¹ correspond to the characteristic stretching and bending modes of the imidazole ring, and C=N in 2-methylimidazole (Hmim), respectively [31]. For Fe₃O₄ NPs (Fig. S1b), the sharp absorption band around 582 cm⁻¹ was attributed to the stretching vibration of Fe—O bonds of Fe₃O₄ NPs. The weak absorption band around 1050 cm⁻¹ is due to the C—O stretching vibration that may be related to the remnants of using *aloe vera* leaves extract. In the case of Ag NPs (Fig. S1c), the FTIR spectra consist of absorption bands correspond to the stretching vibration of C—H, C—O, and C=O bonds attributed to the presence of various phytochemicals in the used extract [32]. In the FTIR spectrum of the PAN polymer (Fig. S1d), the absorption peaks attributed to the vibration of C—H, O—H, C=O, and C≡N bonds were appeared in the range of 400–2300 cm⁻¹. In the M-Ag/PAN/ZIF-67 spectrum (Fig. S1e), all the main absorption bands of ZIF-67 MOFs, Fe₃O₄ NPs, Ag NPs, and PAN polymer are cumulatively visible with a slight shift, which confirms the presence of all their surface functional groups in the nanocomposite structure. Compared to the FTIR spectrum of the M-Ag/PAN/ZIF-67, the FTIR spectrum of M-CuO@Ag/PAN/ZIF-67 (Fig. S1f) show the additional absorption bands at 516 and 620 cm⁻¹, which can be attributed to the CuO stretching vibrations [33], and confirmed that the CuO nanoparticles has successfully doped on nanocomposite structure.

3.1.3. Morphological and elemental composition analysis

The surface morphology and elemental composition of M-CuO@Ag/PAN/ZIF-67 were studied by FESEM-EDX analysis as shown in Fig. 3. The FESEM image (Fig. 3a) show that the M-CuO@Ag/PAN/ZIF-67 structure consisting of nanoparticles with different morphologies and sizes.

The elemental composition of the M-CuO@Ag/PAN/ZIF-67 was investigated as weight percentage by EDX analysis (Fig. 3b). The EDX spectrum reported that the M-CuO@Ag/PAN/ZIF-67 rendered the elements of silver (Ag), carbon (C), cobalt (Co), oxygen (O), copper (Cu), iron (Fe), nitrogen (N), and, which indicates the presence of ZIF-67 MOFs, Fe₃O₄, Ag, and CuO nanoparticles in the nanocomposite structure. Also, the distribution of the elements on the surface of the M-CuO@Ag/PAN/ZIF-67 is presented by the EDX mapping analysis (Fig. 3c). As can be seen, the distribution of elements was almost uniform and elements regions were clearly observed on the nanocomposite surface.

3.1.4. Porosity and textural analysis

The nitrogen adsorption/desorption isotherm (Fig. S2a) of the M-CuO@Ag/PAN/ZIF-67 exhibited a type III isotherm with a type H3 loop, suggesting the presence of the agglomerated solids particles with the non-uniform size and shape [34]. Also, the H3 hysteresis loop is often associated with solids with a very wide distribution of pore size. The pore size distribution (Fig. S2b) was manifested by the BJH method. The result revealed that the prepared sample has a wide range of pore sizes <60 nm, and the BET specific surface area and total pore volume were about 271.8 m² g⁻¹ and 1.0 cm³ g⁻¹, respectively.

3.1.5. Magnetic measurement

The easy separation capability of used adsorbent from the reaction medium is essential for its practical applications. Magnetic separation using a magnet is one of the most accessible methods in this field. The VSM study was used to evaluate the magnetic property of the synthesized M-CuO@Ag/PAN/ZIF-67 at room temperature in the applied field ranging from +10,000 to -10,000 Oe. From the VSM measurement (Fig. S2c), the saturation magnetization (Ms) of M-CuO@Ag/PAN/ZIF-67 and naked Fe₃O₄ nanoparticles were determined 6.20, and 76.73

emu g⁻¹, respectively. The decrease in the Ms. value of the nanocomposite compared to naked Fe₃O₄ nanoparticles was attributed mainly to the low Fe₃O₄ content in the nanocomposite structure. However, this small Ms. value was also quite suitable for easy magnetic separation. Also, the close to zero magnetic remanence and negligible coercivity in the absence of an external magnetic field indicated that the M-CuO@Ag/PAN/ZIF-67 was superparamagnetic [34].

3.1.6. Zeta potential measurement

The surface charge characteristics of the adsorbent plays a key role in the adsorption process. The surface charge characteristic and zero-point charge (pH_{zpc}) of the M-CuO@Ag/PAN/ZIF-67 was calculated by the zeta potential measurement within the pH range from 2 to 12 (Fig. S2d). As can be seen, the zeta potential of the nanocomposite decreased from +15.9 to -27.6 mV with increasing the pH value from 2.0 to 12, indicating that the negative surface charges of the nanocomposite increased within the more alkaline conditions. Also, the pH_{zpc} of nanocomposite was about 6.1 and shows that the adsorbent was positively charged at pH < 6.1 and negatively charged at pH > 6.1. The positive and negative surface charges of the adsorbent will play a very effective role in the formation of repulsion or electrostatic attraction with ACT and PQ at different solution pH and make the role of solution pH in the adsorption process very significant.

3.2. CCD-RSM statistical analysis

The adsorption process was optimized by CCD-RSM statistical analysis along with desirability index, and the adequacy of the model was studied by ANOVA result. In the optimization process, the ANOVA results based on the quadratic model are presented in Table S2. The results showed that the p-values were <0.05, and p-values lack of fit were >0.05, which indicated the predicted model was significant and is able to predict the response for adsorption of ACT and PQ by M-CuO@Ag/PAN/ZIF-67 [35,36]. A summary of the statistical model for the prediction of removal efficiency of ACT and PQ was listed in Table S3. The lower standard deviation mean (SD) values and the closer to 1 of R-Squared (R^2) values indicated that the predicted values are very close to the actual values (response), which is also clearly shown in Fig. S3a-b. Also, the difference between predicted R-Squared and Adjusted R-Squared are <0.2 for both ACT and PQ adsorption and shows that the predicted data are in good agreement with the obtained data [37]. The Adequate Precision (AP) values were above 4 % and Indicated that noise did not cause a response error [38]. The statistical significance of the factors affecting adsorption and determining their importance was shown by considering the line on the Pareto charts in Fig. S3c-d.

As can be seen in the Pareto charts, the most influential factors for the adsorption of ACT and PQ were shown with a longer line and all factors above $p = 0.05$ have been effective in the adsorption process. The simultaneous effects of pH-contact time and pH-adsorbent mass on the removal efficiency of ACT and PQ by M-CuO@Ag/PAN/ZIF-67 were studied by three-dimensional (3D) response surface plots as shown in Fig. 4. The results revealed that the R% ACT (Fig. 4a) was more desirable at higher solution pH and contact times. Also, in general, the R% PQ (Fig. 4b) has increased with increasing of adsorbent mass and solution pH, although the R% PQ decreased slightly with an excessive increase of solution pH value from 8.0 to 11. The simultaneous effects of other experimental conditions on the removal efficiency of ACT and PQ by M-CuO@Ag/PAN/ZIF-67 are shown in Fig. 5. The simultaneous effects of contact time & solution pH (Fig. 5a), and solution temperature & solution pH (Fig. 5b) on R% of ACT are shown and indicated that with increasing solution pH along with increasing contact time and solution temperature, the R% of ACT has increased. This means that the ACT adsorption process was more favorable in alkaline conditions and the increase in contact time and temperature caused more saturation of the empty active sites of the nanocomposite, which results in an increase in the adsorption rate and capacity. Also, the simultaneous effects of the

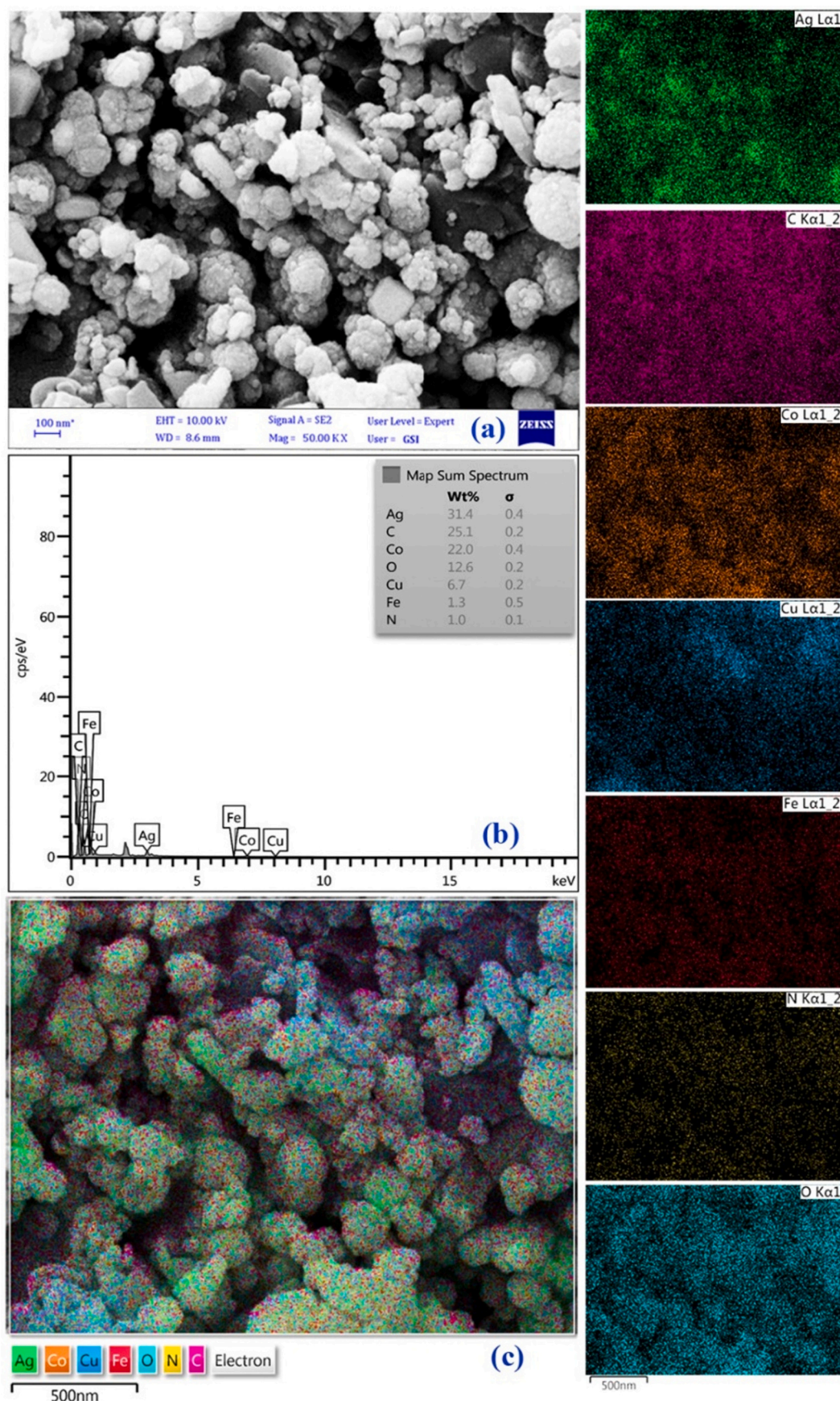


Fig. 3. (a) FESEM image, (b) EDX spectrum, and (c) and elemental mapping of M-CuO@Ag/PAN/ZIF-67.

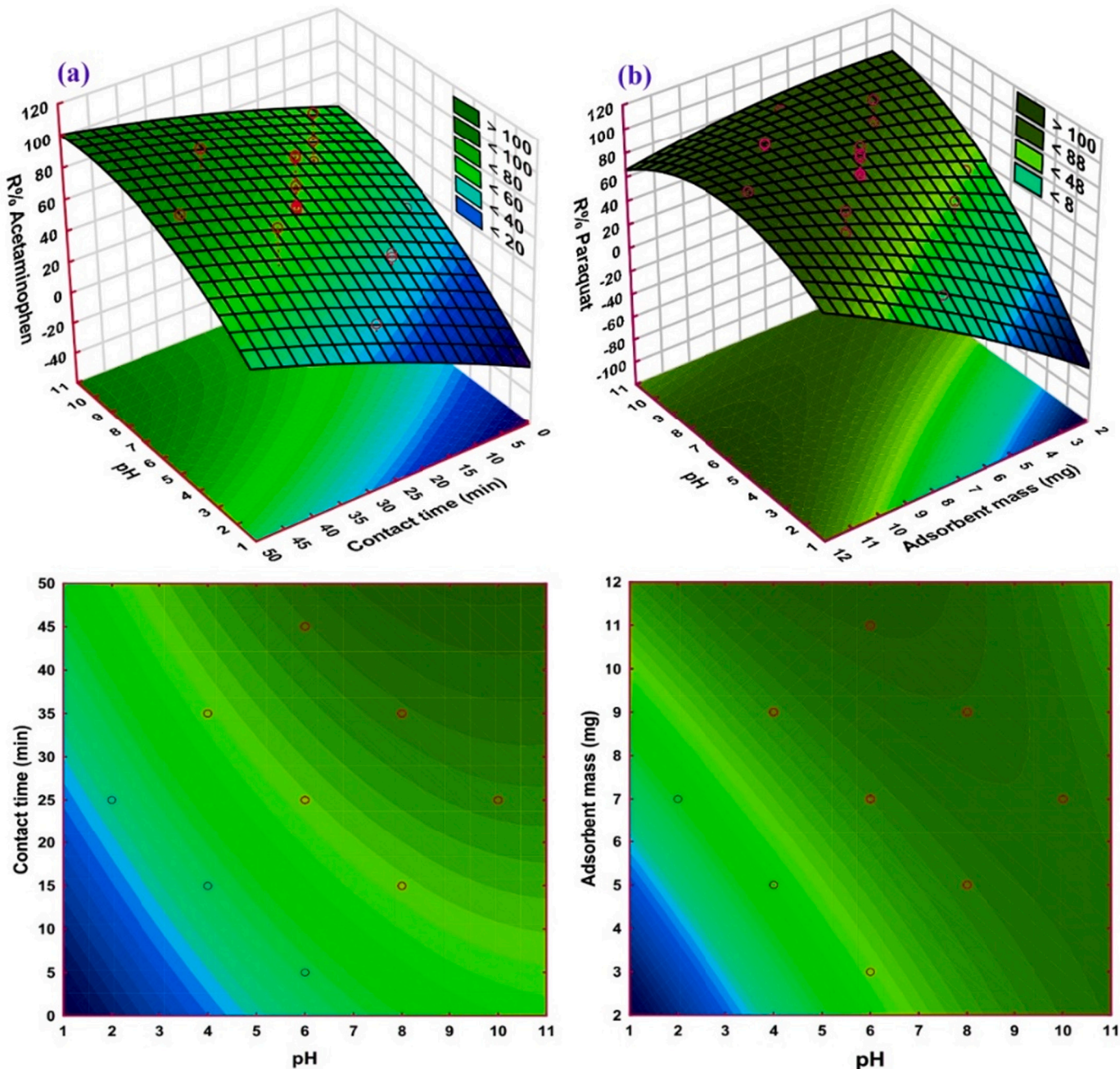


Fig. 4. The 3D response surface and 2D contour plots of the effects the (a) pH and contact time on ACT removal efficiency (R% ACT), and (b) pH and adsorbent mass on PQ removal efficiency (R% PQ) by M-CuO@Ag/PAN/ZIF-67.

initial ACT concentration and the adsorbent mass (Fig. 5c) indicated that the R% of ACT was increased with decreases of ACT initial concentration and increases of adsorbent mass, which can be due to the more availability of active adsorption sites as well as less competition in the uptake of ACT molecules in adsorption process. Also, the simultaneous effects of adsorbent mass & solution pH (Fig. 5c), and contact time & initial PQ concentration (Fig. 5d) on R% of PQ are shown and revealed that generally have similar adsorption behaviors to the ACT adsorption process, which can be due to the approximate proximity of the ACT and PQ chemical structures. Also, the predicted optimal conditions with experimental responses (R%) for adsorptive removal of PQ and ACT by M-CuO@Ag/PAN/ZIF-67 are shown in Table 1. As can be seen, the adsorptive removal optimal conditions are predicted based on 100 % removal efficiency. The obtained average experimental responses (with

5 replications) of removal efficiency for PQ and ACT were 99.23 ± 1.83 and 99.41 ± 2.21 , respectively. The proximity of the experimental data obtained with the predicted values showed the accuracy of the experiment design.

3.3. Adsorption isotherms studies

The equilibrium removal data of ACT and PQ from contaminated water were analyzed using four isotherm models, and their corresponding parameters are given in Table 2. According to the higher correlation coefficients (R^2), the Langmuir isotherm model better described the adsorption process in both PQ ($R^2 = 0.999$) and ACT ($R^2 = 0.999$), which suggesting that the adsorption process was monolayer (chemisorption) and occurred homogeneously [39,40]. Also, the

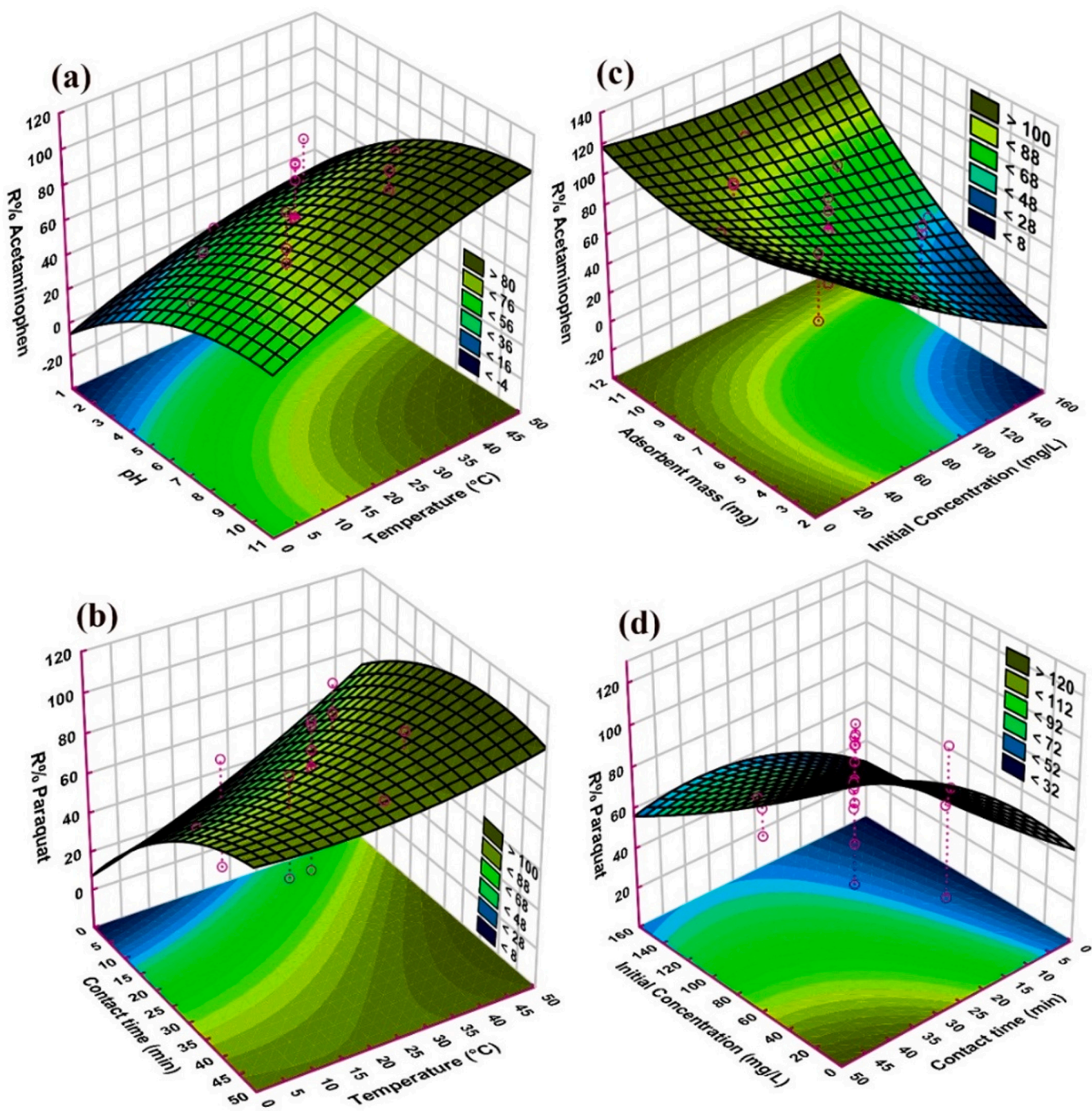


Fig. 5. The 3D response surface plots of the experiment variables on ACT and PQ removal efficiency by M-CuO@Ag/PAN/ZIF-67.

Table 1

Predicted optimal conditions with experimental responses (R%) for adsorptive removal of PQ and ACT.

Variable	Optimum value	
	PQ	ACT
Initial concentration (mg L^{-1})	110	110
pH	8.0	8.0
Adsorbent mass (mg)	7.0	9.0
Sonication time (min)	25	25
Temperature (°C)	35	25
Predicted responses (R%)	100.0	100.0
Experimental responses (R%) ($N = 5$)	99.23 ± 1.83	99.41 ± 2.21

maximum Langmuir monolayer adsorption capacities (Q_m) of PQ and ACT were 1143.7, and 971.6 mg g^{-1} , respectively (Table 3).

The essential characteristics of the Langmuir model can be described by the separation factor (R_L) and indicated that both adsorption of PQ (0.013–0.115) and ACT (0.012–0.111) were favorable ($0 < R_L < 1$). In addition, the energy of adsorption (E) obtained from the D-R isotherm models (2.16, and 2.41 kJ mol^{-1}) were below 8 kJ mol^{-1} , which suggests the physical adsorption process [41]. Therefore, the results of isotherm models showed the participation of both physical and chemical interactions in the adsorptive removal of PQ and ACT by M-CuO@Ag/PAN/ZIF-67.

Table 2

Parameters of adsorption isotherm models for adsorptive removal of PQ and ACT by M-CuO@Ag/PAN/ZIF-67.

Isotherm	Plot	Parameters	PQ	ACT
Langmuir $\frac{C_e}{q_e} = \frac{1}{Q_m k_L} + \frac{C_e}{Q_m k_L}$	C_e/q_e vs. C_e	Q_m (mg g ⁻¹)	1143.7	971.6
		K_L (L mg ⁻¹)	0.386	0.401
		R^2	0.999	0.999
Freundlich $\ln q_e = \ln K_F + \frac{1}{n} \ln C_e$	$\ln q_e$ vs. $\ln C_e$	$R_L = 1/(1 + (K_L \times C_0))$	0.013–0.115	0.012–0.111
		1/n	0.396	0.417
		K_F (L mg ⁻¹)	12.19	11.38
Temkin $q_e = B_1 \ln K_T + \frac{B_1}{B_1 \ln C_e}$	q_e vs. $\ln C_e$	R^2	0.893	0.945
		B_1	205.3	173.3
		K_T (L mg ⁻¹)	1.000	1.000
Dubinin-Radushkevich $\ln q_e = \ln Q_s - \frac{E}{\epsilon^2}$	$\ln q_e$ vs. ϵ^2	R^2	0.946	0.972
		Q_s (mg g ⁻¹)	752.2	614.8
		β	-1.1×10^{-7}	-8.6×10^{-8}
Dubinin-Radushkevich $\ln q_e = \ln Q_s - \frac{E}{\epsilon^2}$	E (kJ mol ⁻¹)	E (kJ mol ⁻¹)	2.161	2.406
		R^2	0.697	0.736

Table 3

Comparison of maximum adsorption capacity (Q_{max}), and contact time reported for PQ and ACT adsorption for different adsorbents.

	Adsorbent	Q_{max} (mg g ⁻¹)	Contact time (min)	Ref.
PQ	Graphene oxide/ mesoporous silica EDTA-induced self-assembly of 3D graphene	31.34 119.0	2 1440	[42] [43]
	Zeolite Y	26.38	1140	[44]
	NaY zeolite	234.4	60	[45]
	Carbon-coated cross-linked PAN fibers	437.6	1440	[46]
	M-CuO@Ag/PAN/ZIF-67	1143.7	25	This work
	Amine functionalized superparamagnetic silica NC	58.00	30	[47]
	AC synthesized from spent tea leaves	59.2	10	[48]
	Silica microspheres	89.0	30	[49]
	Chitosan-coated MWCNT	205	60	[50]
	AC derived from <i>Quercus Brantii</i> (Oak) acorn	45.45	150	[51]
ACT	M-CuO@Ag/PAN/ZIF-67	971.6	25	This work

3.4. Adsorption kinetics and thermodynamics studies

The adsorption kinetics were analyzed by four kinetic models, and their corresponding results were summarized in Table S4. Based on R^2 values, the pseudo-second-order model was most appropriate with experimental data and theoretically adsorbed amounts (q_e) at equilibrium in the pseudo-second-order kinetics model were also close to the adsorbed amount at equilibrium obtained from the experiment. Hence, the results indicated that the chemical adsorption process plays an important role in the adsorptive removal of PQ and ACT by M-CuO@Ag/PAN/ZIF-67 [49]. The adsorption thermodynamic parameters include the standard Gibbs free energy (ΔG°), enthalpy (ΔH°), and entropy change (ΔS°) were calculated by Van't Hoff's plot at different temperatures (278, 288, 298, 308, and 318 K) and results are depicted in Table S5. As can be seen, the positive values of ΔH° were observed for PQ (64.49 kJ mol⁻¹), and ACT (71.91 kJ mol⁻¹) and revealed the endothermic nature of the adsorption process, which means that the adsorption is more desirable at higher temperatures [52]. Also, ΔH° values above 40 kJ mol⁻¹ indicated the presence of chemical interactions in the adsorption process. The negative ΔG° values showed the spontaneous nature of the adsorption process [53], and ΔG° values in the range of 0 to -20 kJ mol⁻¹, revealed that the adsorption process of PQ and ACT occurred more by physical adsorption [54]. In addition,

decreasing ΔG° values with increasing temperature showed that heat promoted the adsorption amount. Furthermore, the positive values of ΔS° exhibited increased randomness along the adsorption process. Therefore, the results of thermodynamic studies showed the cooperation of both physical and chemical interactions in the adsorption process, which was consistent with the results of kinetic studies.

3.5. Identify the adsorption process

The FTIR, UV-Vis, and EDX analysis before and after the adsorption process were used to confirm the adsorptive removal of PQ and ACT by M-CuO@Ag/PAN/ZIF-67. The FTIR and UV-Vis results are shown in Fig. 6. The FTIR analysis of M-CuO@Ag/PAN/ZIF-67 before and after adsorption of PQ (Fig. 6a) and ACT (Fig. 6b) showed that some absorption bands of nanocomposite were shifted to higher/lower wavelengths after the adsorption process. Also, the some new absorption peaks related to ACT and PQ have appeared in the nanocomposite spectrum, which suggesting the involvement of chemical interaction in the adsorption process [55,56]. On the other hand, the ACT and PQ removal from contaminated solutions were justified using UV-Vis measurements before and after the adsorption process. The results showed the absorption intensity of PQ (Fig. 6c), and ACT (Fig. 6d) were decreased significantly, which indicates their very low secondary concentrations in solution after the adsorption process and confirms their effective removal. Also, traces of ACT and PQ absorbed in the M-CuO@Ag/PAN/ZIF-67 were clearly identified by the EDX analysis and are shown in Fig. 7. The EDX analysis after adsorption of ACT (Fig. 7a) shows only an increase in the wt% of nitrogen element and doesn't show any additional element after adsorption.

The EDX result after adsorption of PQ (Fig. 7b) revealed the wt% of nitrogen element (N) has increased and new PQ-related chlorine element (Cl) has appeared, which confirmed the adsorption of PQ on the surface of the nanocomposite. In addition, the element Cl was clearly visible throughout the nanocomposite's surface on the EDX mapping, suggesting that all components of the nanocomposite have been involved in the adsorption process.

3.6. Possible adsorption mechanisms

The possible adsorption mechanisms were explained by isotherm, kinetic and thermodynamic studies. Also, the effects of solution pH on the adsorption efficiency as well as FTIR studies before and after the adsorption process were used to more accurate identification of the existing molecular interactions. In this regard, the monolayer adsorption process, better fit of the pseudo-second-order kinetic model, as well as ΔH° values above 40 kJ mol⁻¹, provides clear evidence of the involvement of chemical interactions in the adsorption process. Also, the appearance of ACT and PQ-related absorption peaks in the adsorbent FTIR spectrum after the adsorption process was another evidence of the occurrence of chemical adsorption. Reciprocally, the energy of adsorption (E) values obtained from the D-R isotherm models were below 8 kJ mol⁻¹, and ΔG° values were in the range of 0 to -20 kJ mol⁻¹ suggested the physical adsorption process. Therefore, the possible adsorption mechanisms of ACT and PQ by M-CuO@Ag/PAN/ZIF-67 can be considered as the combination of physical and chemical interactions. On the other hand, the significant effect of solution pH on the adsorption efficiency of ACT and PQ, which is attributed to the surface charge of the adsorbent showed that the electrostatic interactions had a major role in the adsorption process. Also, the molecular structures of ACT and PQ showed that their aromatic rings have the ability to interact π - π interactions with the ZIF-67 MOFs aromatic rings in the adsorbent structure. In addition, the presence of oxygen-containing surface functional groups in the nanocomposite and ACT/PQ structures, and their absorption peak shifts in the FTIR after the adsorption process also evidence the possibility of adsorption through hydrogen bonds. In this regard, hydrogen bonds, electrostatic attractions, and π - π interactions

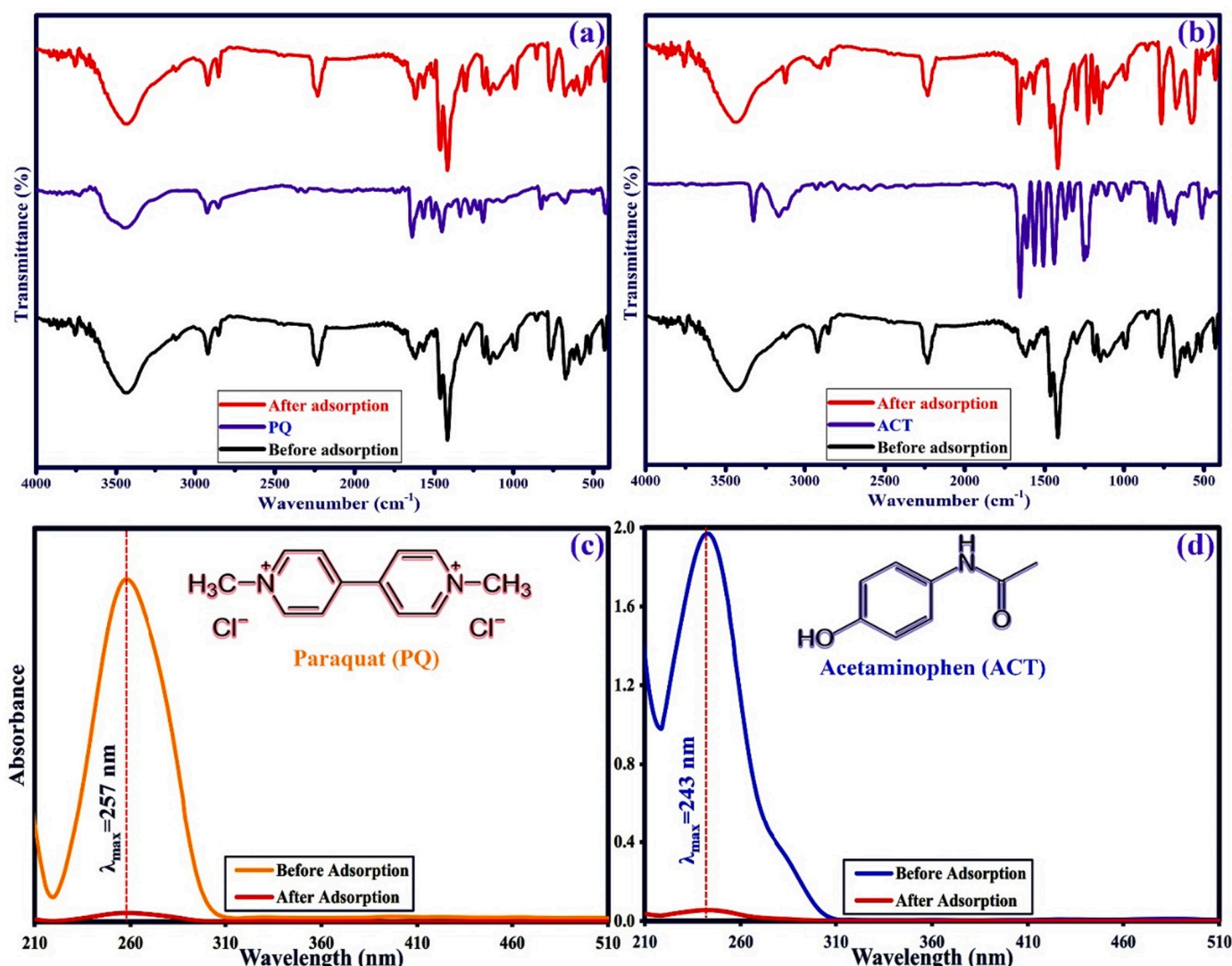


Fig. 6. FTIR spectra of M-CuO@Ag/PAN/ZIF-67 before and after adsorptive removal of (a) PQ, and (b) ACT. The UV-Vis spectra of (c) PQ-contaminated solution, and (d) ACT-contaminated solution before and after adsorption process.

may be major mechanisms of ACT and PQ adsorption by the M-CuO@Ag/PAN/ZIF-67.

3.7. Antibacterial activity

The antibacterial activity of M-CuO@Ag/PAN/ZIF-67 on *E. coli*, *S. aureus*, and *B. subtilis* bacteria was examined by pour plate (Fig. 8) and disc diffusion (Fig. 9) methods. As can be seen in digital images of the pour plate method (Fig. 8a-c), the Petri dishes with untreated bacteria (as the control group) were seen as cloudy. In these images, cloudy agar medium indicates the massive growth of bacteria. The relevant FESEM images (Fig. 8d-i) also clearly show the untreated bacteria morphologies, indicating that the bacteria are without any damage in their morphology.

The digital images of the bacteria after co-culture with M-CuO@Ag/PAN/ZIF-67 for 24 h (Fig. 8j-l) show that the agar culture medium remained transparent and they are not cloudy. The transparency of the agar culture medium indicated the lack of mass growth of bacteria and showed that the bacteria have not been grown in the presence of the nanocomposite. Also, the relevant FESEM images (Fig. 8m-r) clearly shows the deposition of nanocomposite in bacteria and some of the bacteria have suffered destruction in their structure. The antibacterial

studies of the M-CuO@Ag/PAN/ZIF-67 and their raw materials by disc diffusion method were also evaluated based on the amount of inhibitory zone (created shadow) formed around the paper disks impregnated with them. The related digital images are shown in Fig. 9a, and the results are summarized in Fig. 9b. The results showed that the M-CuO@Ag/PAN/ZIF-67 has a more effective antibacterial effect than its components based on their inhibitory zone (*E. coli*: 2 mm, *S. aureus*: 5 mm, and *B. subtilis*: 6 mm), which may be due to the synergy and intensification of antibacterial properties of the components together. Also, it is shown that using CuO nanoparticles in the nanocomposite structure has enhanced the antibacterial effect of the composite. *Escherichia coli*'s greater resistance to the antibacterial properties of the composite may be due to the presence of that outer lipid membrane, which positive bacteria lack [2,57]. On the other hand, the surface of bacteria such as *Staphylococcus aureus* contains surface functional groups such as amines and carboxyl. These functional groups cause these bacteria to show a higher affinity for CuO and other metal oxide nanoparticles [58]. In addition, the antibacterial activity of the nanocomposite may be accredited to the generation of enhanced stages of reactive oxygen species (ROS) and the deposition of nanocomposite on the surface of the bacteria [59,60].

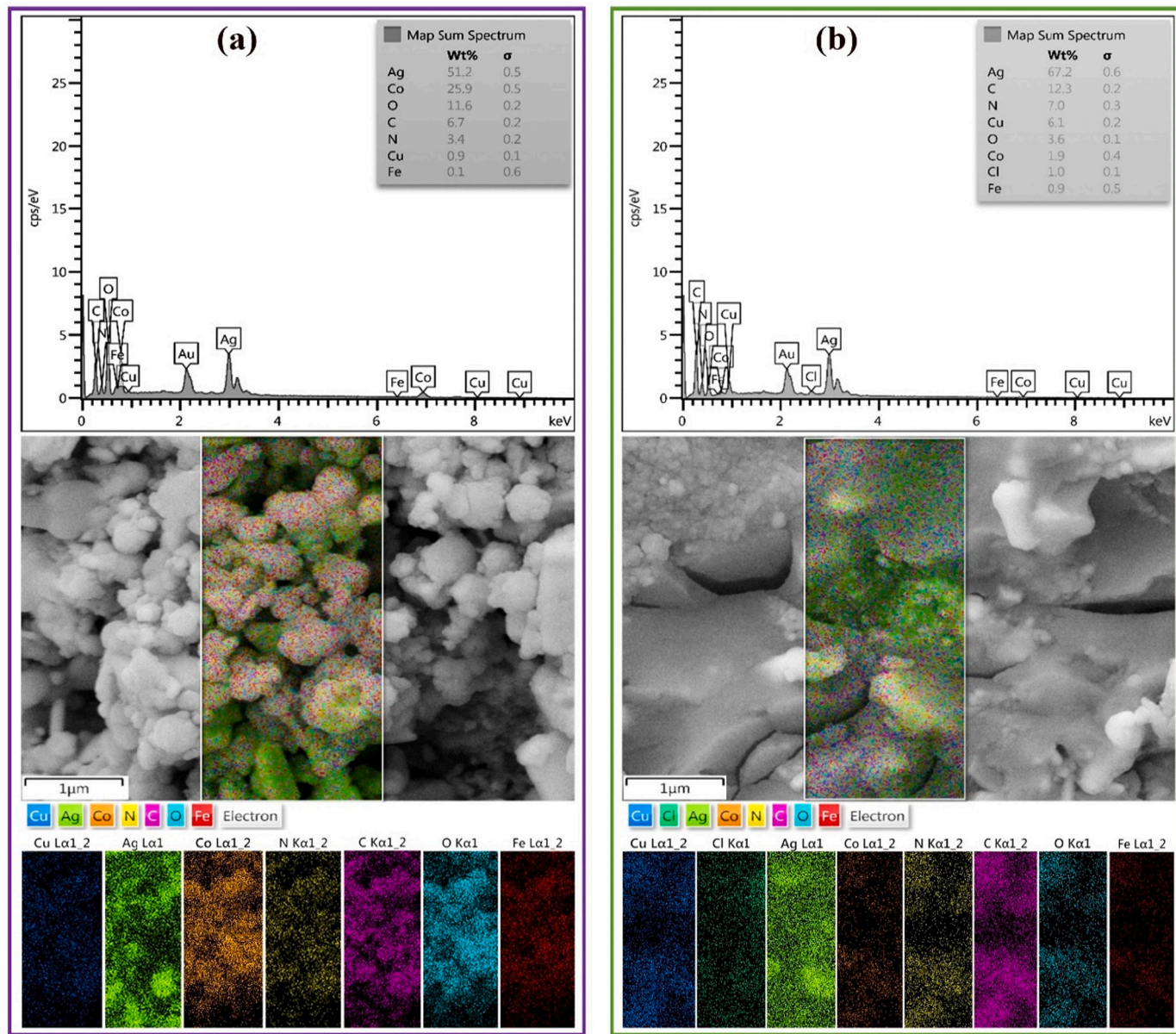


Fig. 7. EDX spectrum and elemental mapping of the M-CuO@Ag/PAN/ZIF-67 after adsorptive removal of (a) ACT, and (b) PQ from contaminated water.

3.8. Recycling of the adsorbent

The reusability and stability of an antibacterial adsorbent are necessary factors for its cost-effectiveness. For this purpose, after each experiment, the spent adsorbent was easily collected from the reaction medium by a small magnet and regenerated by washing with methanol and chlorination method. The effectiveness of methanol in desorption of PQ and ACT is consistent with the results of other reports [61,62]. Then, the regenerated adsorbent was washed with ultrapure water and was dried at 50 °C for subsequent cycle reuse. The reusability test results are given in Fig. S4. As can be seen in Fig. S4a, the M-CuO@Ag/PAN/ZIF-67 was able to remove about 90 % of ACT and 80 % of PQ from contaminated waters in the 7th reuse cycle, and the reduction in adsorption efficiency may have been due to incomplete adsorbent regeneration and also saturation of some active adsorption sites. In addition, the reusability test result for antibacterial properties of M-CuO@Ag/PAN/ZIF-67 was shown in Fig. S4b. The result showed that the bacterial reduction efficiency has remained above 90 % until the 7th reuse cycle. Therefore, the results showed that the M-CuO@Ag/PAN/ZIF-67 is an effective and

economical candidate as an antibacterial adsorbent that can be used for water treatment purposes.

3.9. Practical efficiency of adsorbent

The practical efficiency of adsorbent was explored for the removal of PQ and ACT from the real water samples including tap water, and river water. Initially, the water samples were filtered through the Whatman no. 42 filter paper and then the initial concentrations of PQ and ACT in these waters were measured and adjusted to 110 mg L⁻¹. After that, the adsorption process was taken under optimum conditions and the residual concentrations of PQ and ACT were measured. The results showed that the removal efficiency of adsorbent in tap water for PQ and ACT was 91 % and 95 %, respectively. Also, the removal efficiency of PQ and ACT in river water was 82 % and 86 %, respectively. The result indicated that the adsorbent showed excellent performance in real water samples.

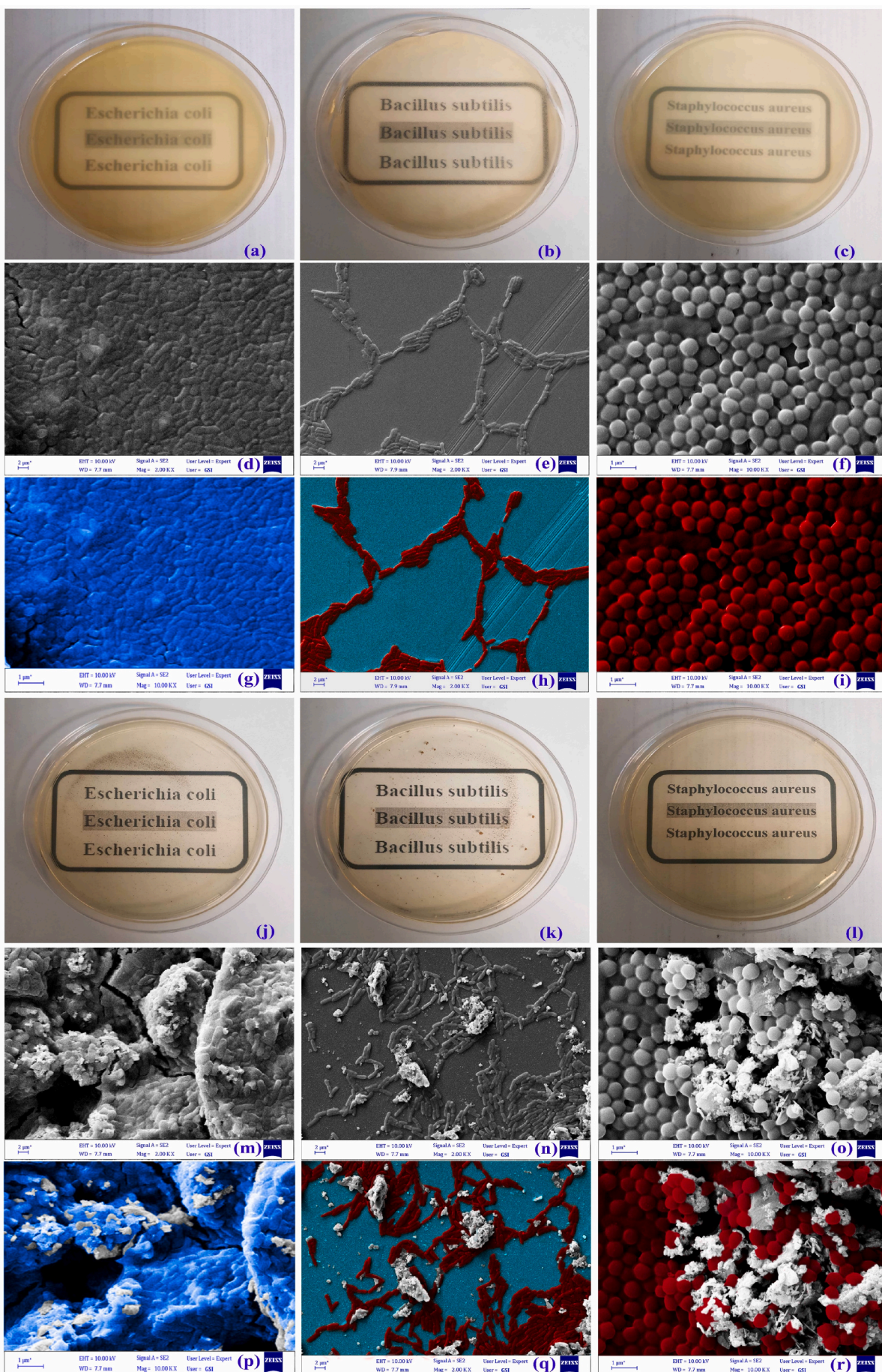


Fig. 8. The antibacterial efficiency study of the M-CuO@Ag/PAN/ZIF-67 for *E. coli*, *B. subtilis*, and *S. aureus* bacteria (1.0×10^9 CFU/mL) by pour plate method: (a-c) Digital images of Petri dishes with untreated bacteria cultivated on MHA agar as the control sample, (d-i) FESEM images of the untreated bacteria, (j-l) Digital images of Petri dishes of treated bacteria by the co-cultured with M-CuO@Ag/PAN/ZIF-67, (m-r) FESEM images of the treated bacteria.

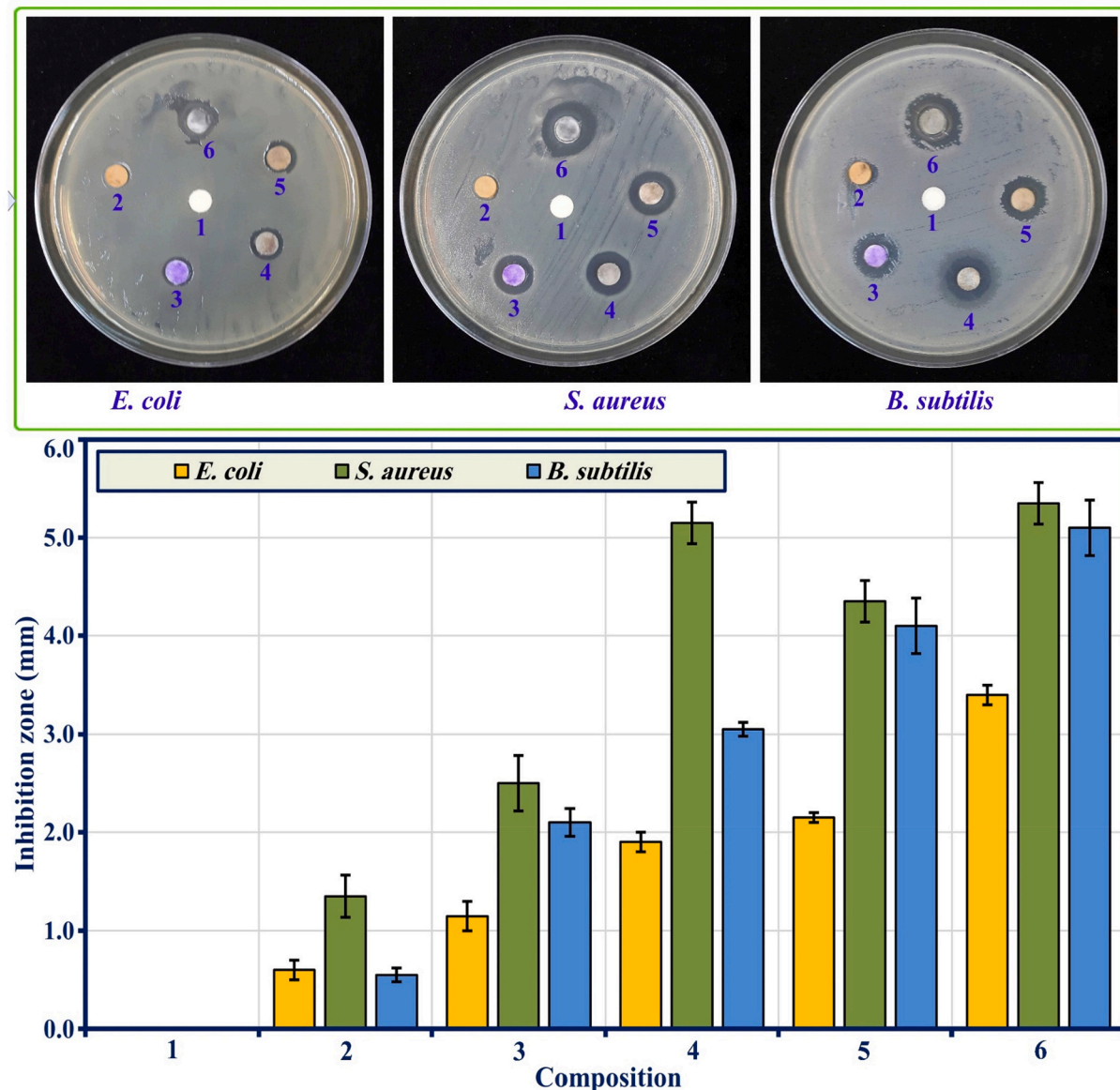


Fig. 9. (a) The antibacterial efficiency study of (1) blank, (2) Fe_3O_4 NPs, (3) ZIF-67 MOFs, (4) Ag NPs, (5) M-ZIF-67/PAN/Ag, and (6) M-CuO@Ag/PAN/ZIF-67 for *E. coli*, *B. subtilis*, and *S. aureus* bacteria by disc diffusion method. (b) Inhibition zone results of disc diffusion method for prepared samples against *E. coli*, *B. subtilis*, and *S. aureus* bacteria.

4. Conclusion

In this work, a multifunctional M-CuO@Ag/PAN/ZIF-67 was synthesized in the presence of herbal aqueous extracts and was characterized in detail by XRD, FTIR, FESEM-EDX, BET-BJH, VSM, and zeta potential analysis. The ability of the synthesized nanocomposite to adsorptive removal of acetaminophen and paraquat from contaminated water as well as its antibacterial properties on *S. aureus*, *B. subtilis*, and *E. coli* bacteria were evaluated. The model and optimize the adsorption process were performed based on maximizing removal efficiency of ACT and PQ from aqueous solutions. According to this, CCD-RSM was used and the significance of independent variables and their interactions were tested by the analysis of variance (ANOVA). The adsorption results showed that the M-CuO@Ag/PAN/ZIF-67 was able to remove $99.41 \pm$

2.21% of ACT and $99.23 \pm 1.83\%$ of PQ from contaminated water under optimal conditions and the maximum Langmuir monolayer adsorption capacities for ACT and PQ were 971.6 and 1143.7 mg g^{-1} , respectively. The absorption of ACT and PQ by M-CuO@Ag/PAN/ZIF-67 was well confirmed by FTIR, EDX mapping and UV-Vis analysis. The antibacterial properties of M-CuO@Ag/PAN/ZIF-67 was studied by pour plate and disk diffusion methods on Gram-positive *S. aureus* and *B. subtilis* bacteria, and Gram-negative *E. coli* bacterium. The results showed that the bacterial suppression by nanocomposite was effective in both Gram-positive and Gram-negative bacteria; nevertheless, showed more effectiveness in Gram-positive bacteria. Also, it concluded that the collective antibacterial effects of the nanocomposite are stronger than its components and copper-doped has also strengthened the antibacterial properties.

Declaration of competing interest

The authors declare that they have no known competing financial interests or personal relationships that could have appeared to influence the work reported in this paper.

Data availability

The authors do not have permission to share data.

Acknowledgments

The authors acknowledge the financial support from the Yasuj University of Medical Sciences (IR.YUMS.REC.1399.164), Yasuj, Iran.

Appendix A. Supplementary data

Supplementary data to this article can be found online at <https://doi.org/10.1016/j.jwpe.2022.103025>.

References

- [1] H.B. Quesada, L.F. Cusiolli, C. de O Bezerra, A.T.A. Baptista, L. Nishi, R.G. Gomes, R. Bergamasco, Acetaminophen adsorption using a low-cost adsorbent prepared from modified residues of *Moringa oleifera* Lam. seed husks, *J. Chem. Technol. Biotechnol.* 94 (2019) 3147–3157, <https://doi.org/10.1002/jctb.6121>.
- [2] M.H. Abu Elella, E.S. Goda, H. Gamal, S.M. El-Bahy, M.A. Nour, K.R. Yoon, Green antimicrobial adsorbent containing grafted xanthan gum/SiO₂ nanocomposites for malachite green dye, *Int. J. Biol. Macromol.* 191 (2021) 385–395, <https://doi.org/10.1016/j.ijbiomac.2021.09.040>.
- [3] J. Źur, D. Wojciechyska, K. Hupert-Kocurek, A. Marchlewicz, U. Guzik, Paracetamol – toxicity and microbial utilization. *Pseudomonas moorei* KB₄ as a case study for exploring degradation pathway, *Chemosphere* 206 (2018) 192–202, <https://doi.org/10.1016/j.chemosphere.2018.04.179>.
- [4] S. Ahmadzadeh, M. Dolatabadi, Removal of acetaminophen from hospital wastewater using electro-Fenton process, *Environ. Earth Sci.* 77 (2018) 53, <https://doi.org/10.1007/s12665-017-7203-7>.
- [5] N.K. Hamadi, S. Sri, X.D. Chen, Adsorption of paraquat dichloride from aqueous solution by activated carbon derived from used tires, *J. Hazard. Mater.* 112 (2004) 133–141, <https://doi.org/10.1016/j.jhazmat.2004.04.011>.
- [6] W.T. Tsai, C.W. Lai, K.J. Hsien, Effect of particle size of activated clay on the adsorption of paraquat from aqueous solution, *J. Colloid Interface Sci.* 263 (2003) 29–34, [https://doi.org/10.1016/S0021-9797\(03\)00213-3](https://doi.org/10.1016/S0021-9797(03)00213-3).
- [7] S.-T. Hsu, T.-C. Pan, Adsorption of paraquat using methacrylic acid-modified rice husk, *Bioresour. Technol.* 98 (2007) 3617–3621, <https://doi.org/10.1016/j.biortech.2006.11.060>.
- [8] D. Atsmania, M. Hamadache, S. Hanini, O. Benkortbi, D. Oukrif, Prediction of the antibacterial activity of garlic extract on *E. coli*, *S. aureus* and *B. subtilis* by determining the diameter of the inhibition zones using artificial neural networks, *LWT - Food Sci. Technol.* 82 (2017) 287–295, <https://doi.org/10.1016/j.lwt.2017.04.053>.
- [9] H. Naeem, M. Ajmal, R.B. Qureshi, S.T. Muntha, M. Farooq, M. Siddiq, Facile synthesis of graphene oxide–silver nanocomposite for decontamination of water from multiple pollutants by adsorption, catalysis and antibacterial activity, *J. Environ. Manag.* 230 (2019) 199–211, <https://doi.org/10.1016/j.jenvman.2018.09.061>.
- [10] K.Y. Kumar, T.N.V. Raj, S. Archana, S.B.B. Prasad, S. Olivera, H.B. Muralidhara, SnO₂ nanoparticles as effective adsorbents for the removal of cadmium and lead from aqueous solution: adsorption mechanism and kinetic studies, *J. Water Process Eng.* 13 (2016) 44–52, <https://doi.org/10.1016/j.jwpe.2016.07.007>.
- [11] M.H. Abu Elella, E.S. Goda, H.M. Abdallah, A.E. Shalan, H. Gamal, K.R. Yoon, Innovative bactericidal adsorbents containing modified xanthan gum/montmorillonite nanocomposites for wastewater treatment, *Int. J. Biol. Macromol.* 167 (2021) 1113–1125, <https://doi.org/10.1016/j.ijbiomac.2020.11.065>.
- [12] M.R. Azhar, H.R. Abid, V. Periasamy, H. Sun, M.O. Tade, S. Wang, Adsorptive removal of antibiotic sulfonamide by UiO-66 and ZIF-67 for wastewater treatment, *J. Colloid Interface Sci.* 500 (2017) 88–95, <https://doi.org/10.1016/j.jcis.2017.04.001>.
- [13] Y. Yang, S. Zhang, W. Huang, Z. Guo, J. Huang, H. Yang, D. Ye, W. Xu, S. Gu, Multi-functional cotton textiles design using in situ generating zeolitic imidazolate framework-67 (ZIF-67) for effective UV resistance, antibacterial activity, and self-cleaning, *Cellulose* 28 (2021) 5923–5935, <https://doi.org/10.1007/s10570-021-03840-8>.
- [14] S. Sathyavimal, S. Vasantharaj, D. Bharathi, M. Saravanan, E. Manikandan, S. S. Kumar, A. Pugazhendhi, Biogenesis of copper oxide nanoparticles (CuO-NPs) using *Sida acuta* and their incorporation over cotton fabrics to prevent the pathogenicity of gram negative and gram positive bacteria, *J. Photochem. Photobiol. B* 188 (2018) 126–134, <https://doi.org/10.1016/j.jphotobiol.2018.09.014>.
- [15] S. Tang, J. Zheng, Antibacterial activity of silver nanoparticles: structural effects, *Adv. Healthc. Mater.* 7 (2018), 1701503, <https://doi.org/10.1002/adhm.201701503>.
- [16] P. Hajipour, A. Bahrami, A. Esfami, A. Hosseini-Abari, H.R. Hagh Ranjbar, Chemical bath synthesis of CuO-GO-Ag nanocomposites with enhanced antibacterial properties, *J. Alloys Compd.* 821 (2020), 153456, <https://doi.org/10.1016/j.jallcom.2019.153456>.
- [17] X. He, D.-P. Yang, X. Zhang, M. Liu, Z. Kang, C. Lin, N. Jia, R. Luque, Waste eggshell membrane-templated CuO-ZnO nanocomposites with enhanced adsorption, catalysis and antibacterial properties for water purification, *Chem. Eng. J.* 369 (2019) 621–633, <https://doi.org/10.1016/j.cej.2019.03.047>.
- [18] N. Ghasemi, F. Jamali-Sheini, R. Zekavati, CuO and Ag/CuO nanoparticles: biosynthesis and antibacterial properties, *Mater. Lett.* 196 (2017) 78–82, <https://doi.org/10.1016/j.matlet.2017.02.111>.
- [19] E. Alipanahpour Dil, M. Ghaedi, A. Asfaram, F. Mehrabi, F. Sadeghfari, Efficient adsorption of azore B onto CNTs/ZnO@Ni₂P-NCs from aqueous solution in the presence of ultrasound wave based on multivariate optimization, *J. Ind. Eng. Chem.* 74 (2019) 55–62, <https://doi.org/10.1016/j.jiec.2018.12.050>.
- [20] K.Y. Kumar, H. Muralidhara, Y.A. Nayaka, J. Balasubramanyam, H. Hanumanthappa, Low-cost synthesis of metal oxide nanoparticles and their application in adsorption of commercial dye and heavy metal ion in aqueous solution, *Powder Technol.* 246 (2013) 125–136, <https://doi.org/10.1016/j.powtec.2013.05.017>.
- [21] A. Asfaram, M. Ghaedi, H. Javadian, A. Goudarzi, Cu- and S-@SnO₂ nanoparticles loaded on activated carbon for efficient ultrasound assisted dispersive μSPE-spectrophotometric detection of quercetin in *Nasturtium officinale* extract and fruit juice samples: CCD-RSM design, *Ultrason. Sonochem.* 47 (2018) 1–9, <https://doi.org/10.1016/j.ultrsonch.2018.04.008>.
- [22] R. Bagheri, M. Ghaedi, A. Asfaram, E. Alipanahpour Dil, H. Javadian, RSM-CCD design of malachite green adsorption onto activated carbon with multimodal pore size distribution prepared from *amygdalus scoparia*: kinetic and isotherm studies, *Polyhedron* 171 (2019) 464–472, <https://doi.org/10.1016/j.poly.2019.07.037>.
- [23] L. Upadhyaya, B. Oliveira, V.J. Pereira, M.T. Barreto Crespo, J.G. Crespo, D. Quemener, M. Semsarilar, Nanocomposite membranes from nano-particles prepared by polymerization induced self-assembly and their biocidal activity, *Sep. Purif. Technol.* 251 (2020), 117375, <https://doi.org/10.1016/j.separpur.2020.117375>.
- [24] G. Gu, J. Xu, Y. Wu, M. Chen, L. Wu, Synthesis and antibacterial property of hollow SiO₂/Ag nanocomposite spheres, *J. Colloid Interface Sci.* 359 (2011) 327–333, <https://doi.org/10.1016/j.jcis.2011.04.002>.
- [25] O.L. Galkina, K. Önneby, P. Huang, V.K. Ivanov, A.V. Agafonov, G.A. Seisenbaeva, V.G. Kessler, Antibacterial and photochemical properties of cellulose nanofiber-titania nanocomposites loaded with two different types of antibiotic medicines, *J. Mater. Chem. B* 3 (2015) 7125–7134, <https://doi.org/10.1039/C5TB01382H>.
- [26] J. Qian, F. Sun, L. Qin, Hydrothermal synthesis of zeolitic imidazolate framework-67 (ZIF-67) nanocrystals, *Mater. Lett.* 82 (2012) 220–223, <https://doi.org/10.1016/j.matlet.2012.05.077>.
- [27] J. Liu, R. Che, H. Chen, F. Zhang, F. Xia, Q. Wu, M. Wang, Microwave absorption enhancement of multifunctional composite microspheres with spinel Fe₃O₄ cores and anatase TiO₂ shells, *Small* 8 (2012) 1214–1221, <https://doi.org/10.1002/smll.201102245>.
- [28] O. Zuas, N. Hamim, Y. Sampora, Bio-synthesis of silver nanoparticles using water extract of *myrmecodia pendan* (Sarang semut plant), *Mater. Lett.* 123 (2014) 156–159, <https://doi.org/10.1016/j.matlet.2014.03.026>.
- [29] S. Chatterjee, A. Ray, M. Mandal, S. Das, S.K. Bhattacharya, Synthesis and characterization of CuO-NiO nanocomposites for electrochemical supercapacitors, *J. Mater. Eng. Perform.* 29 (2020) 8036–8048, <https://doi.org/10.1007/s11665-020-05261-3>.
- [30] U. Holzwarth, N. Gibson, The scherrer equation versus the 'Debye-scherrer equation', *Nat. Nanotechnol.* 6 (2011) <https://doi.org/10.1038/nnano.2011.145>, 534–534.
- [31] M. Ammar, S. Jiang, S. Ji, Heteropoly acid encapsulated into zeolite imidazolate framework (ZIF-67) cage as an efficient heterogeneous catalyst for friedel-crafts acylation, *J. Solid State Chem.* 233 (2016) 303–310, <https://doi.org/10.1016/j.jssc.2015.11.014>.
- [32] K. Varghese Alex, P. Tamil Pavai, R. Rugmini, M. Shiva Prasad, K. Kamakshi, K. C. Sekhar, Green synthesized Ag nanoparticles for bio-sensing and photocatalytic applications, *ACS Omega* 5 (2020) 13123–13129, <https://doi.org/10.1021/acsomega.0c01136>.
- [33] A. Umar, A.A. Ibrahim, H. Algadi, U.T. Nakate, S.P. Choudhury, T. Alsuwian, H. Albargi, M.A. Alsaifi, S. Baskoutas, Selective ethanol gas sensing performance of flower-shaped CuO composed of thin nanoplates, *J. Mater. Sci. Mater. Electron.* 32 (2021) 18565–18579, <https://doi.org/10.1007/s10854-021-06249-y>.
- [34] Z. Mosayebi, M. Rezaei, N. Hadian, F.Z. Kordshuli, F. Meshkani, Low temperature synthesis of nanocrystalline magnesium aluminate with high surface area by surfactant assisted precipitation method: effect of preparation conditions, *Mater. Res. Bull.* 47 (2012) 2154–2160, <https://doi.org/10.1016/j.materresbull.2012.06.010>.
- [35] P. Arabkhani, H. Javadian, A. Asfaram, S.N. Hosseini, A reusable mesoporous adsorbent for efficient treatment of hazardous triphenylmethane dye wastewater: RSM-CCD optimization and rapid microwave-assisted regeneration, *Sci. Rep.* 11 (2021) 22751, <https://doi.org/10.1038/s41598-021-02213-2>.
- [36] A. Asfaram, E.A. Dil, P. Arabkhani, F. Sadeghfari, M. Ghaedi, Magnetic cu: CuO-GO nanocomposite for efficient dispersive micro-solid phase extraction of polycyclic aromatic hydrocarbons from vegetable, fruit, and environmental water samples by

- liquid chromatographic determination, *Talanta* 218 (2020), <https://doi.org/10.1016/j.talanta.2020.121131>.
- [37] E.Alipanahpour Dil, M. Ghaedi, A. Asfaram, F. Mehrabi, A.A. Bazrafshan, L. Tayebi, Synthesis and application of Ce-doped TiO₂ nanoparticles loaded on activated carbon for ultrasound-assisted adsorption of Basic Red 46 dye, *Ultrason. Sonochem.* 58 (2019), 104702, <https://doi.org/10.1016/j.ulsonch.2019.104702>.
- [38] H. Motaghi, P. Arabkhani, M. Parvinnia, A. Asfaram, Simultaneous adsorption of cobalt ions, azo dye, and imidacloprid pesticide on the magnetic chitosan/activated carbon@UiO-66 bio-nanocomposite: optimization, mechanisms, regeneration, and application, *Sep. Purif. Technol.* 284 (2022), 120258, <https://doi.org/10.1016/j.seppur.2021.120258>.
- [39] P. Arabkhani, H. Javadian, A. Asfaram, F. Sadeghfar, F. Sadegh, Synthesis of magnetic tungsten disulfide/carbon nanotubes nanocomposite (WS₂/Fe₃O₄/CNTs-NC) for highly efficient ultrasound-assisted rapid removal of amaranth and brilliant blue FCF hazardous dyes, *J. Hazard. Mater.* 420 (2021), 126644, <https://doi.org/10.1016/j.jhazmat.2021.126644>.
- [40] Y. Rashtbari, S. Hazrati, A. Azari, S. Afshin, M. Fazlzadeh, M. Vosoughi, A novel, eco-friendly and green synthesis of PPAC-ZnO and PPAC-nZVI nanocomposite using pomegranate peel: cephalixin adsorption experiments, mechanisms, isotherms and kinetics, *Adv. Powder Technol.* 31 (2020) 1612–1623, <https://doi.org/10.1016/j.appt.2020.02.001>.
- [41] V.S. Munagapati, D.S. Kim, Equilibrium isotherms, kinetics, and thermodynamics studies for Congo red adsorption using calcium alginate beads impregnated with nano-goethite, *Ecotoxicol. Environ. Saf.* 141 (2017) 226–234, <https://doi.org/10.1016/j.ecoenv.2017.03.036>.
- [42] Z. Dehghani, M. Sedghi-Asl, M. Ghaedi, M.M. Sabzehmeidani, E. Adhami, Ultrasound-assisted adsorption of paraquat herbicide from aqueous solution by graphene oxide/ mesoporous silica, *J. Environ. Chem. Eng.* 9 (2021), 105043, <https://doi.org/10.1016/j.jeche.2021.105043>.
- [43] Y. Huang, C. Li, Z. Lin, EDTA-induced self-assembly of 3D graphene and its superior adsorption ability for paraquat using a teabag, *ACS Appl. Mater. Interfaces* 6 (2014) 19766–19773, <https://doi.org/10.1021/am504922v>.
- [44] R. Sirival, N. Patdhaganul, S. Preechararn, S. Photharin, Removal of paraquat solution onto zeolite material, in: *AIP Conf. Proc.*, AIP Publishing LLC, 2018, p. 030006.
- [45] C. Keawkumay, W. Rongchapoo, N. Sosa, S. Suthirakun, I.Z. Koleva, H. A. Aleksandrov, G.N. Vayssilov, J. Wittayakun, Paraquat adsorption on NaY zeolite at various Si/Al ratios: a combined experimental and computational study, *Mater. Chem. Phys.* 238 (2019), 121824, <https://doi.org/10.1016/j.matchemphys.2019.121824>.
- [46] R. Zhao, Y. Wang, X. Li, B. Sun, Y. Li, H. Ji, J. Qiu, C. Wang, Surface activated hydrothermal carbon-coated electrospun PAN fiber membrane with enhanced adsorption properties for herbicide, *ACS Sust. Chem. Eng.* 4 (2016) 2584–2592, <https://doi.org/10.1021/acssuschemeng.6b00026>.
- [47] S. Chandrashekhar Kollarahithlu, R.M. Balakrishnan, Adsorption of pharmaceutical pollutants, ibuprofen, acetaminophen, and streptomycin from the aqueous phase using amine functionalized superparamagnetic silica nanocomposite, *J. Clean. Product.* 294 (2021), 126155, <https://doi.org/10.1016/j.jclepro.2021.126155>.
- [48] S. Wong, Y. Lim, N. Ngadi, R. Mat, O. Hassan, I.M. Intuwa, N.B. Mohamed, J. H. Low, Removal of acetaminophen by activated carbon synthesized from spent tea leaves: equilibrium, kinetics and thermodynamics studies, *Powder Technol.* 338 (2018) 878–886, <https://doi.org/10.1016/j.powtec.2018.07.075>.
- [49] R. Natarajan, K. Banerjee, P.S. Kumar, T. Somanna, D. Tannani, V. Arvind, R.I. Raj, D.-V.N. Vo, K. Saikia, V.K. Vaidyanathan, Performance study on adsorptive removal of acetaminophen from wastewater using silica microspheres: kinetic and isotherm studies, *Chemosphere* 272 (2021), 129896, <https://doi.org/10.1016/j.chemosphere.2021.129896>.
- [50] L. Yanyan, T.A. Kurniawan, A.B. Albadarin, G. Walker, Enhanced removal of acetaminophen from synthetic wastewater using multi-walled carbon nanotubes (MWCNTs) chemically modified with NaOH, HNO₃/H₂SO₄, ozone, and/or chitosan, *J. Mol. Liq.* 251 (2018) 369–377, <https://doi.org/10.1016/j.molliq.2017.12.051>.
- [51] H. Nourmoradi, K.F. Moghadam, A. Jafari, B. Kamarehie, Removal of acetaminophen and ibuprofen from aqueous solutions by activated carbon derived from *quercus brantii* (Oak) acorn as a low-cost biosorbent, *J. Environ. Chem. Eng.* 6 (2018) 6807–6815, <https://doi.org/10.1016/j.jece.2018.10.047>.
- [52] A. Rasaie, M.M. Sabzehmeidani, M. Ghaedi, M. Ghane-Jahromi, A. Sedarati-Jahromi, Removal of herbicide paraquat from aqueous solutions by bentonite modified with mesoporous silica, *Mater. Chem. Phys.* 262 (2021), 124296, <https://doi.org/10.1016/j.matchemphys.2021.124296>.
- [53] A.A. Basaleh, M.H. Al-Malack, T.A. Saleh, Methylene blue removal using polyamide-vermiculite nanocomposites: kinetics, equilibrium and thermodynamic study, *J. Environ. Chem. Eng.* 7 (2019), 103107, <https://doi.org/10.1016/j.jece.2019.103107>.
- [54] B.-Y. Yang, Y. Cao, F.-F. Qi, X.-Q. Li, Q. Xu, Atrazine adsorption removal with nylon6/polypyrrole core-shell nanofibers mat: possible mechanism and characteristics, *Nanoscal. Res. Lett.* 10 (2015) 207, <https://doi.org/10.1186/s11671-015-0903-6>.
- [55] P. Arabkhani, H. Javadian, A. Asfaram, M. Ateia, Decorating graphene oxide with zeolitic imidazolate framework (ZIF-8) and pseudo-boehmite offers ultra-high adsorption capacity of diclofenac in hospital effluents, *Chemosphere* 271 (2021), 129610, <https://doi.org/10.1016/j.chemosphere.2021.129610>.
- [56] P. Arabkhani, A. Asfaram, M. Ateia, Easy-to-prepare graphene oxide/sodium montmorillonite polymer nanocomposite with enhanced adsorption performance, *J. Water Process Eng.* 38 (2020), <https://doi.org/10.1016/j.jwpe.2020.101651>.
- [57] L. Brown, J.M. Wolf, R. Prados-Rosales, A. Casadevall, Through the wall: extracellular vesicles in gram-positive bacteria, mycobacteria and fungi, *Nat. Rev. Microbiol.* 13 (2015) 620–630, <https://doi.org/10.1038/nrmicro3480>.
- [58] A.A. Menazea, M.K. Ahmed, Silver and copper oxide nanoparticles-decorated graphene oxide via pulsed laser ablation technique: preparation, characterization, and photoactivated antibacterial activity, *Nano-Struct. Nano-Object.* 22 (2020), 100464, <https://doi.org/10.1016/j.nanoso.2020.100464>.
- [59] V. Shanmugam, K.S. Jeyaperumal, Investigations of visible light driven sn and cu doped ZnO hybrid nanoparticles for photocatalytic performance and antibacterial activity, *Appl. Surf. Sci.* 449 (2018) 617–630, <https://doi.org/10.1016/j.apsusc.2017.11.167>.
- [60] Z.A. Khan, E.S. Goda, A. Ur Rehman, M. Sohail, Selective antimicrobial and antibiofilm activity of metal-organic framework NH₂-MIL-125 against *Staphylococcus aureus*, *Mater. Sci. Eng. B* 269 (2021), 115146, <https://doi.org/10.1016/j.mseb.2021.115146>.
- [61] A. Mojiri, M. Vakili, H. Farraj, S.Q. Aziz, Combined ozone oxidation process and adsorption methods for the removal of acetaminophen and amoxicillin from aqueous solution; kinetic and optimisation, *Environ. Technol. Innov.* 15 (2019), 100404, <https://doi.org/10.1016/j.eti.2019.100404>.
- [62] D. Shetty, S. Boutros, T. Skorjanc, B. Garai, Z. Asfari, J. Raya, A. Trabolsi, Fast and efficient removal of paraquat in water by porous polycalix[n]arenes (n = 4, 6, and 8), *J. Mater. Chem. A* 8 (2020) 13942–13945, <https://doi.org/10.1039/DOTA01907K>.